2nd Advanced Optical Metrology Compendium

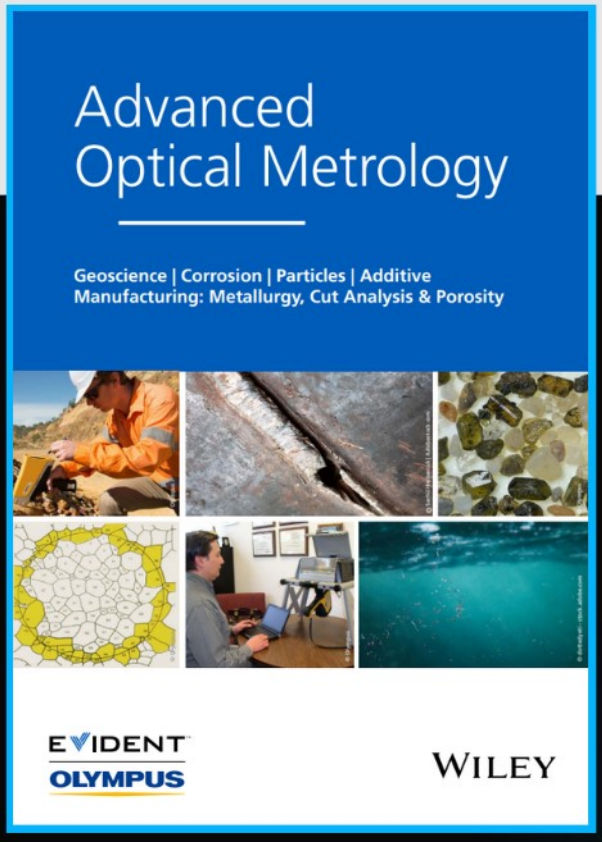

The latest eBook from Advanced Optical Metrology. Download for free.

This compendium includes a collection of optical metrology papers, a repository of teaching materials, and instructions on how to publish scientific achievements.

With the aim of improving communication between fundamental research and industrial applications in the field of optical metrology we have collected and organized existing information and made it more accessible and useful for researchers and practitioners.

EVIDENT
OLYMPUS

WILEY

NANO · MICRO small
www.small-journal.com

Strain Regulating and Kinetics Accelerating of Micro-Sized Silicon Anodes via Dual-Size Hollow Graphitic Carbons Conductive Additives

*Qitao Shi, Yuanhao Cheng, Jiaqi Wang, Junhua Zhou, Huy Quang Ta, Xueyu Lian, Klaudia Kurtyka, Barbara Trzebicka, Thomas Gemming, and Mark H. Rümmeli**

Micro-sized silicon (μSi) anode features fewer interfacial side reactions and lower costs compared to nanosized silicon, and has higher commercial value when applied as a lithium-ion battery (LIB) anode. However, the high localized stress generated during (de)lithiation causes electrode breakdown and performance deterioration of the μSi anode. In this work, hollow graphitic carbons with tailored dual sizes are employed as conductive additives for the μSi anode to overcome electrode failure. The dual-size hollow graphitic carbons (HGC) additives consist of particles with micrometer size similar to the μSi particles; these additives are used for strain regulation. Additionally, nanometer-size particles similar to commercial carbon black Spheron (SP) are used mainly for kinetics acceleration. In addition to building an efficient conductive network, the dual-size hollow graphitic carbon conductive additive prevents the fracture of the electrode by reducing local stress and alleviating volume expansion. The μSi anode with dual-size hollow graphitic carbons as conductive additives achieves an impressive capacity of 651.4 mAh g^{-1} after 500 cycles at a high current density of 2 A g^{-1}. These findings suggest that dual-size hollow graphitic carbons are expected to be superior conductive additives for micro-sized alloy anodes similar to μSi.

1. Introduction

Rechargeable secondary batteries are playing an increasingly significant role in modern society. There is a great demand for lithium-ion batteries for use in applications such as consumer electronics, portable laptops, and renewable energy vehicles.[1–3] Unfortunately, the commercial graphite anode with a theoretical capacity of 372 mAh g^{-1} cannot meet the growing demands placed on lithium-ion batteries (LIB). Therefore, the development of next-generation anode materials with higher capacity has become imperative. Compared to commercial graphite, alloy anode materials possess higher theoretical lithium storage capacity (2–10 times higher) and lower working potential. The emerging alloy anodes include Si, Sn, Ge, and Al.[4–6] Among the alternative anode materials, Si has attracted the most attention in both academia and industry due to its extremely high theoretical capacity of 3759 mAh g^{-1} (at room temperature), as well as its abundant resources, relatively low Li uptake voltage, low cost, and environmental friendliness.[7–10]

Despite the attractive advantages mentioned above, the commercialization of Si anode still faces numerous difficulties that are mainly caused by the dramatic volume change and intrinsic sluggish dynamics during the electrochemical process.[11] These negative effects are greatly magnified with the increase in the material size.[12] Nanostructured Si has been proven to be effective in alleviating volume expansion and enhancing electrode

Q. Shi, Y. Cheng, J. Wang, J. Zhou, H. Q. Ta, X. Lian, M. H. Rümmeli
Soochow Institute for Energy and Materials InnovationS
College of Energy
Key Laboratory of Advanced Carbon Materials and Wearable Energy Technologies of Jiangsu Province
Key Laboratory of Core Technology of High Specific Energy Battery and Key Materials for Petroleum and Chemical Industry
Soochow University
Suzhou 215006, Suzhou 215006, China
E-mail: m.ruemmeli@ifw-dresden.de

The ORCID identification number(s) for the author(s) of this article can be found under https://doi.org/10.1002/smll.202205284.

DOI: 10.1002/smll.202205284

Q. Shi, Y. Cheng, J. Wang, J. Zhou, H. Q. Ta, X. Lian, M. H. Rümmeli
Jiangsu Key Laboratory of Advanced Negative Carbon Technologies
Soochow University
Suzhou, Jiangsu 215123, P. R. China

H. Q. Ta, M. H. Rümmeli
Institute for Complex Materials
IFW Dresden
20 Helmholtz Strasse, 01069 Dresden, Germany

K. Kurtyka, B. Trzebicka, T. Gemming, M. H. Rümmeli
Centre of Polymer and Carbon Materials
Polish Academy of Sciences
M. Curie-Sklodowskiej 34, Zabrze 41–819, Poland

M. H. Rümmeli
Institute of Environmental Technology
VSB-Technical University of Ostrava
17. Listopadu 15, Ostrava 70833, Czech Republic

conductivity.[13] Nevertheless, the troublesome interfacial side reactions caused by the large surface area and the high cost of the synthesis and manufacturing of nanosized Si prevent its use in practical applications. By contrast, micro-sized Si (μSi) benefits from its fewer electrochemical side reactions and lower production cost when considered for use as an anode material for lithium ion batteries.[14] However, the volume change of μSi will result in rapid electrode cracking. To date, various strategies have been proposed to solve the above-mentioned problems, including material structure design,[15–17] carbon compositing,[14,18–20] electrolyte modification,[21,22] and functional binder exploitation.[23–26]

Exploration and improvement of conductive additives have been barely mentioned in the previous research on μSi anodes. The reported conductive additives in lithium secondary battery area in recent years can be generally divided into the following categories: carbon materials, such as 0D carbon black spheron (SP),[27,28] 1D carbon nanotubes,[29,30] 2D graphitic carbons[31–33] and 3D graphite,[34] and other kinds of materials such as Ti_4O_7[35] and Cu nanowires.[36] All of the above conductive additives are expected to affect the μSi electrode solely by proving better electrical connections.

Hollow graphitic carbons have been extensively reported as anode materials for alkali metal ion batteries.[37–39] However, the hollow architecture will lead to a low volumetric energy density, which is unfavorable for practical applications. To rationally take advantage of hollow graphitic carbons and compensate for the inadequacy of research on conductive additives, we propose novel hollow graphitic carbons (HGC) with tailored dual sizes as functional conductive additives. The tailored dual sizes are the micrometer size which is similar to the size of the μSi particles and the nanometer size which is similar to the size of the particles of the commercial carbon black SP conductive additive. The micro-sized hollow graphitic carbons (μHGC) act to realize a rational distribution of μSi particles and alleviate local space expansion due to their dimensional similarity and natural elasticity. On the other hand, the nanosized hollow graphitic carbons (nHGC) provide abundant contact points to enhance the overall conductivity of the μSi electrode due to superior electron transport. With the assistance of the dual-size hollow graphitic carbons conductive additives (μHGC + nHGC), μSi anode shows stable electron and ion transport and enhanced lithium storage and exhibits a satisfactory capacity of 651.4 mAh g^{-1} after 500 cycles at a high current density of 2 A g^{-1}, which is far better than that of the μSi electrode with SP as the conductive additive. Ex situ electrochemical impedance spectra (EIS), Raman spectra, and electron microscopy were employed to elucidate the advanced functions of the dual-size HGC additives in μSi electrodes, confirming its suitability and superiority for use as a conductive additive for μSi (alloy) anodes.

2. Results and Discussion

2.1. Materials Characterization

The morphologies of the as-purchased μSi particles, SP, the as-synthesized micro-sized hollow graphitic carbons, and nanosized graphitic carbons were examined by scanning electron microscopy (SEM) and transmission electron microscopy (TEM). Figure S1a (Supporting Information) shows the micro-sized bulk structures of the Si particles and their size distributions are displayed in Figure S1b (Supporting Information). An examination of **Figure 1**a confirms that the size of μHGC is similar to that of Si. The morphologies of nHGC and SP are exhibited in Figure 1b,c, in which the difference between the hollow structure and the solid structure is shown visually. It is speculated that with the same weight ratio in the electrode, nHGC will occupy more space in the electrode and will construct a more effective conductive network than SP. The TEM image of nHGC vividly depicts the 3D hollow structure with thin graphitic layers (Figure 1e) that promotes elasticity. HRTEM image of SP shows the graphitic lattice with a solid structure (Figure 1f). Figure 1g–i show the size distributions of the above-mentioned μHGC, nHGC, and SP additives which are in accordance with our design.

X-ray diffraction spectra were used to analyze the graphitic structure. The XRD patterns of the μHGC, nHGC, and SP additives exhibit broad peaks at ≈21.6° (**Figure 2**a), corresponding to the (0 0 2) plane of graphitic carbon. The difference between their peak intensities implies that μHGC, nHGC has more disordered areas than SP, which is beneficial for electrolyte penetration and transport. The Raman spectra presented in Figure 2b show the structural information of μHGC, nHGC, and SP and exhibit two peaks centered at 1346 and 1579 cm^{-1} that is indexed to the D band (defect feature) and G band (graphitic feature), respectively. The D/G intensity ratio of SP (1.24) clearly exceeds that of μHGC (1.13) and nHGC (1.08), suggesting that μHGC and nHGC possess a higher degree of graphitization, which is conducive to fast electron transport. The XRD pattern and Raman spectrum of μSi are also provided in the supplementary materials (Figure S2, Supporting Information).

The N_2 adsorption/desorption isotherm curves of μHGC, nHGC, and SP additives display a type-IV shape (Figure 2c), indicating the existence of mesopores and macropores. Figure 2d shows the pore size distributions of the above carbon additives. The mesopores with diameters in the 1–10 nm range account for most of the pores in the three samples. μHGC has more pores with diameters >100 nm than nHGC and SP because it is synthesized on a micro-sized MgO template (Figure S3, Supporting Information). For the solid SP, the pore size varies from 1–110 nm, possibly due to the agglomeration of the SP nanoparticles (Figure S4, Supporting Information). μHGC and nHGC have specific surface areas of 308.4 and 590.3 $m^2 g^{-1}$, respectively, which are much larger than that of SP (62.7 $m^2 g^{-1}$). The high surface area can promote electrolyte penetration as extensively reported.

2.2. Electrode Evaluation

Figure 3a plots the particles configurations of the μSi, μHGC and nHGC additives in the designed μHGC + nHGC@μSi electrode (note that the electrode is named as conductive additives@μSi, for example, μHGC + nHGC@μSi means μSi electrode with μHGC and nHGC as conductive additives), where the μHGC particles are dispersed between the μSi particles to reduce the local agglomeration of μSi, and nHGC particles are

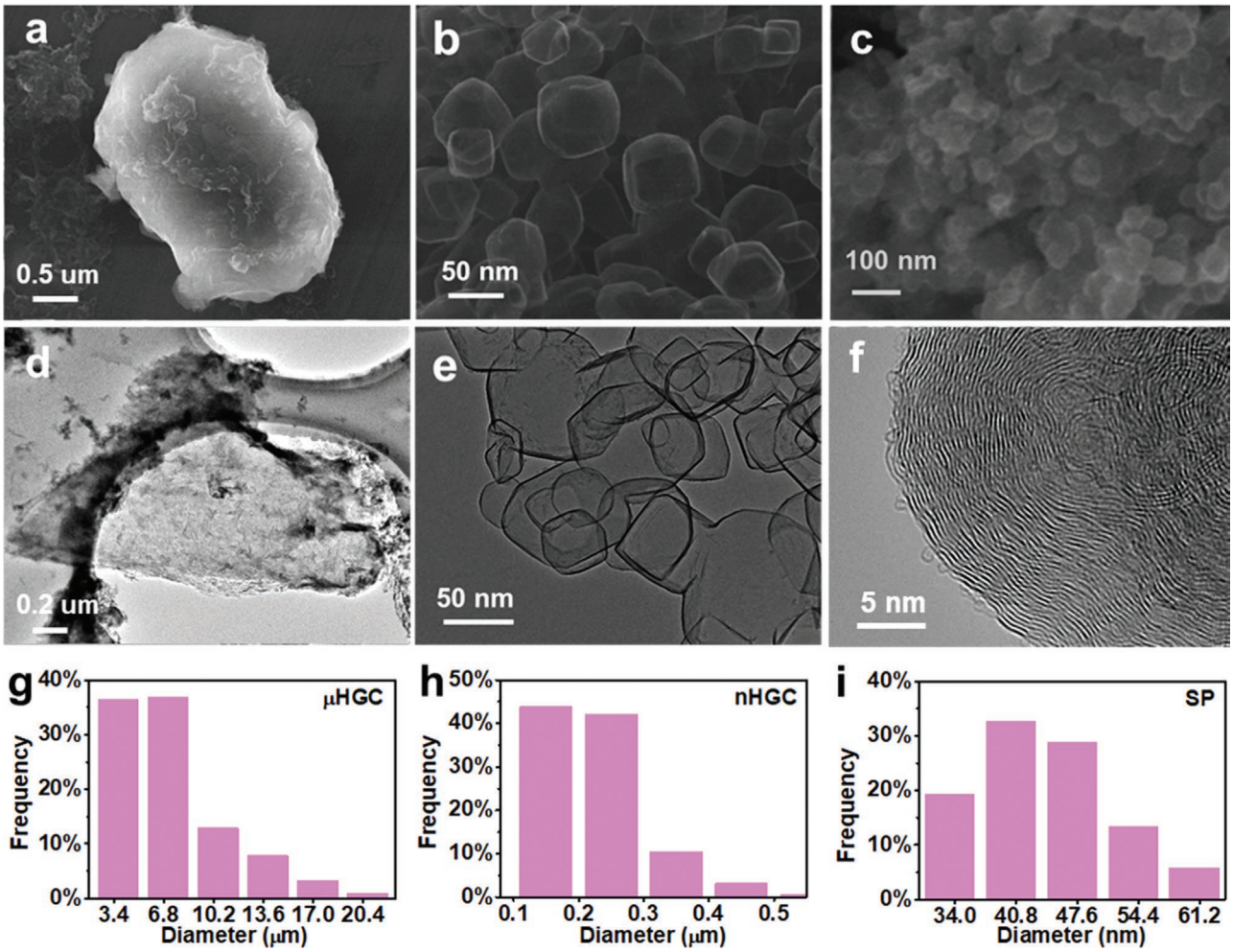

Figure 1. SEM images of a) micro-sized hollow graphitic carbons (μHGC). b) nano-sized hollow graphitic carbons (nHGC) and c) commercial conductive additives SP. TEM images of d) μHGC, e) nHGC and f) SP. size distributions of g) μHGC, h) nHGC and i) SP.

located at the gaps between the micro-sized particles to build a highly-interconnected conductive network. Figure 3d depicts the distributions of the μSi and SP particles in the SP@μSi electrode, where μSi particles are dispersed more densely and tend to cause more severe strain during lithiation. A comparison of the SEM images of the μHGC + nHGC@μSi and SP@μSi electrodes (Figure 3b,e) shows that the μSi particles are distributed to a greater extent in the μHGC + nHGC@μSi electrode, confirming that μHGC additives effectively regulate the μSi configuration within the binder network. We further measured the EDS mapping of the Si element (purple area) to better show the Si distributions in both electrodes. Consistent with the assumed configuration in Figure 3a,d, we proposed that μSi in the mapping area shows less agglomeration in the μHGC + nHGC@μSi electrode, as more no-Si regions are located between μSi; these can be either μHGC or pores. This is not found in the SP@μSi electrode.

To validate our design and evaluate the advantages of dual-size conductive additives, we first performed EIS measurements for both electrodes in the fresh state. The Nyquist plots for both electrodes are shown in **Figure 4**a. The semicircle in the high-frequency region normally represents the charge transfer resistance (R_{ct}) that is associated with Li-ion migration through the electrolyte, separator, and solid electrolyte interface. The μHGC + nHGC@μSi anode in the fresh state exhibit a semicircle with a smaller radius than that of the fresh SP@μSi anode, pointing to the weaker R_{ct} enabled by dual-size HGC additives.

The oblique line in the low-frequency range represents the Li-ion diffusion impedance within the electrode materials, known as the Warburg impedance (W_s). Furthermore, the Li-ion diffusion coefficient (D_{Li^+}) can be calculated using the following equations,[40,41]

$$D_{Li^+} = \frac{R^2T^2}{2A^2n^4F^4C^2\sigma^2} \quad (1)$$

$$C = \frac{n}{V} = \frac{(m/M)}{V} = \frac{\rho V/M}{V} = \frac{\rho}{M} \quad (2)$$

where R is the gas constant (8.314 J K^{-1} mol^{-1}), T is room temperature (298 K), A is the electrode surface area (1.98 cm^2), n is the number of electrons transferred during the reaction, F is the Faraday constant (96 500 C mol^{-1}), C is the molar concentration of Li^+ in the electrode that can be calculated from

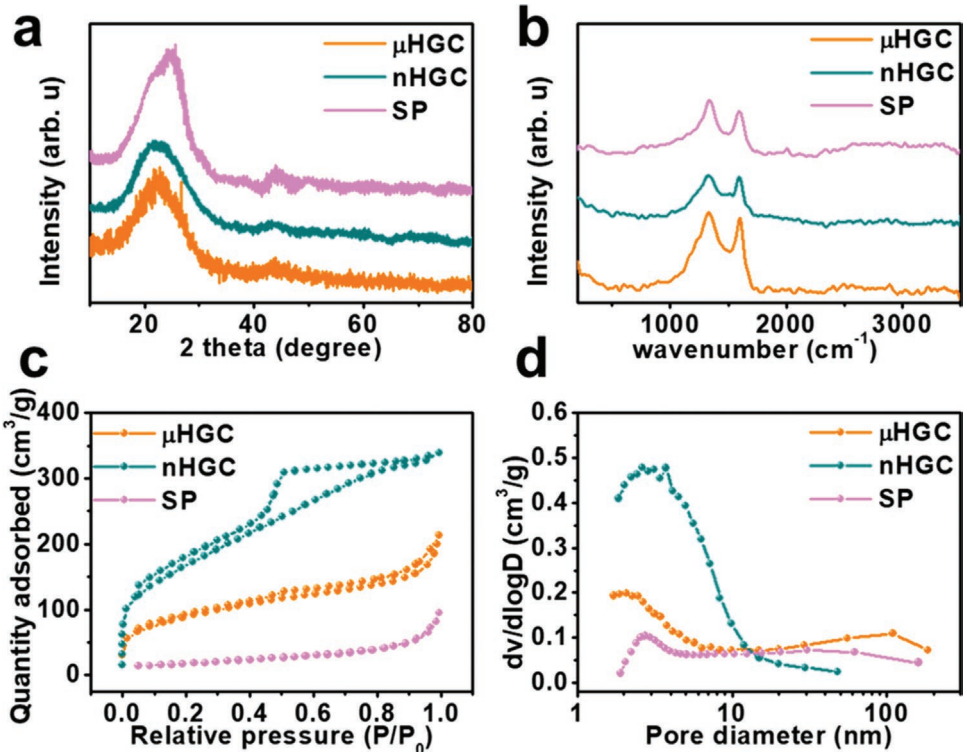

Figure 2. a) XRD measurements, b) Raman spectra, c) BET-specific area measurements and d) pore volume distributions of μHGC, nHGC, and SP.

Equation (2), and σ is the Warburg coefficient that is equal to the slope of the $Z \approx \omega^{-1/2}$ plot presented in Figure 4b. In Equation (2), ρ and M are the molar mass of the electrode material (28 g mol^{-1} for Si) and the tap density (0.43 g cm^{-3}). Considering that the dual-size hollow graphitic carbons are only used as conductive additives, the active material in electrodes should only be that of silicon. In this work, we merely replace the SP additives in the SP@μSi anode with the dual-size HGC additives, with the exception of the Warburg coefficient σ, the variables in the D_{Li}^+ formula are identical for both electrodes. Thus, the difference between the D_{Li}^+ values of the two anodes depends on σ. The D_{Li}^+ of the μHGC + nHGC@μSi anode is 8.19×10^{-15} cm^2 s^{-1}, which is three times higher than that of the SP@μSi anode (1.76×10^{-15} cm^2 s^{-1}). As a control, we also

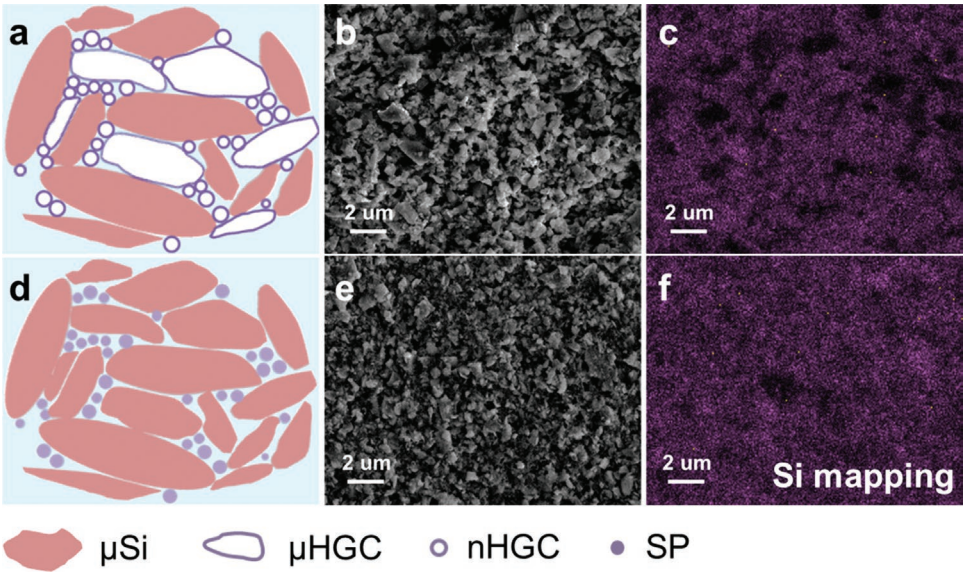

Figure 3. a) Schematic of the μSi, μHGC and nHGC particles' distributions in the μHGC + nHGC@μSi electrode. d) Schematic of the μSi and SP particles' distributions in the SP@μSi electrode. SEM images of b) the μHGC + nHGC@μSi electrode and e) the SP@μSi electrode. Si element EDS mapping of c) the μHGC + nHGC@μSi electrode and f) the SP@μSi electrode.

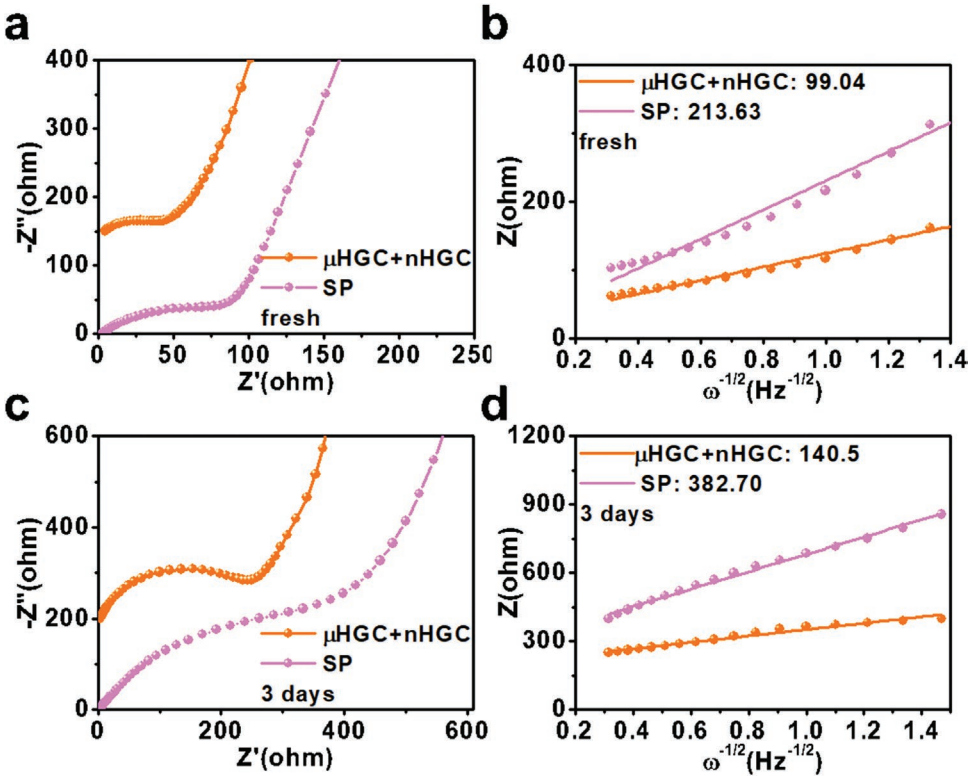

Figure 4. EIS measurements of μHGC + nHGC@μSi and SP@μSi anodes a) at the fresh state and c) after 3-day calendar aging. relationship between Z and $\omega^{-1/2}$ at low frequencies of the μHGC + nHGC@μSi and SP@μSi anodes b) at the fresh state and d) after 3-day calendar aging.

prepared a μSi electrode with μHGC or nHGC as conductive additives. The results of the EIS measurements of the μHGC@μSi anode and the nHGC@μSi anode are plotted in Figure S5 (Supporting Information). It is observed that in a fresh cell, nHGC additives are more effective for reducing the impedance because of their nano size that allows them to fill more gaps and create more contact points between the μSi particles.

Furthermore, EIS measurements of the cells after 3-day calendar aging were carried out. It was found that the impedance of the μHGC + nHGC@μSi anode shows a smaller increase than the SP@μSi anode. The Warburg coefficients of the aged μHGC + nHGC@μSi anode and the SP@μSi anode increase to 140.5 and 382.70, corresponding to the Li^+ diffusion coefficients decline to 4.180×10^{-15} cm^2 s^{-1} and 0.549×10^{-15} cm^2 s^{-1}, respectively. The increase in the electrode resistance and the deceleration of Li^+ diffusion can be ascribed to the formation of the SEI layer that blocks electron and ion transport. Moreover, the kinetics of the μHGC + nHGC@μSi anode shows less decay because the dual-size HGC builds a more effective conductive network and absorbs electrolyte preferentially due to its high specific surface. Thus, dual-size HGC conductive additive successfully improves the electrode capability against calendar aging, suggesting its potential for enabling prolonged service life.

2.3. Electrochemical Performance

The electrochemical properties of a μSi anode with dual-size HGC and SP as conductive additives were evaluated as shown in **Figure 5**. Cyclic voltammetry for the initial three cycles in the voltage window of 0.01 to 2 V at a scan rate of 0.1 mV s^{-1} was applied to examine the electrochemical reaction of the μHGC + nHGC@μSi anode (Figure 5a). An irreversible reduction peak at below 0.1 V was observed during the first cathodic scanning but disappeared in the subsequent cycles, which is attributed to the lithiation of the crystalline Si to generate a Li-Si alloy.[42] The Li-Si alloy is delithiated to amorphous Si during the first anodic scanning, resulting in two oxidation peaks at ≈0.4 and 0.52 V. In addition, the reduction peaks that shift to 0.2 V in the subsequent cycles correspond to the transformation of amorphous Si to Li_xSi, indicating that crystalline Si cannot be regenerated from the Li-Si alloy during electrochemical oxidation. As a control, the SP@μSi anode shows similar electrochemical reactions in the first three cycles (Figure S6, Supporting Information). Figure 5b exhibits the galvanostatic charge/discharge profiles of both electrodes at the first, 10th, and 50th cycle, in which the curves for μHGC + nHGC@μSi anode are marked with hollow circles and the curves for SP@μSi anode are marked with solid circles. The voltage platforms during charge/discharge are consistent with the observed CV profiles. In addition to the electrochemical properties revealed in the voltage profiles, the profiles also enable a clear evaluation of the electrode stability. Although the initial capacity of the μHGC + nHGC@μSi anode is slightly lower than that of the SP@μSi anode, the performance of the μHGC + nHGC@μSi anode quickly surpasses that of the SP@μSi anode at the 10th cycle and then shows a steadily increasing difference, showing a considerable advantage of ≈400 mAh g^{-1} at the 50th cycle. The

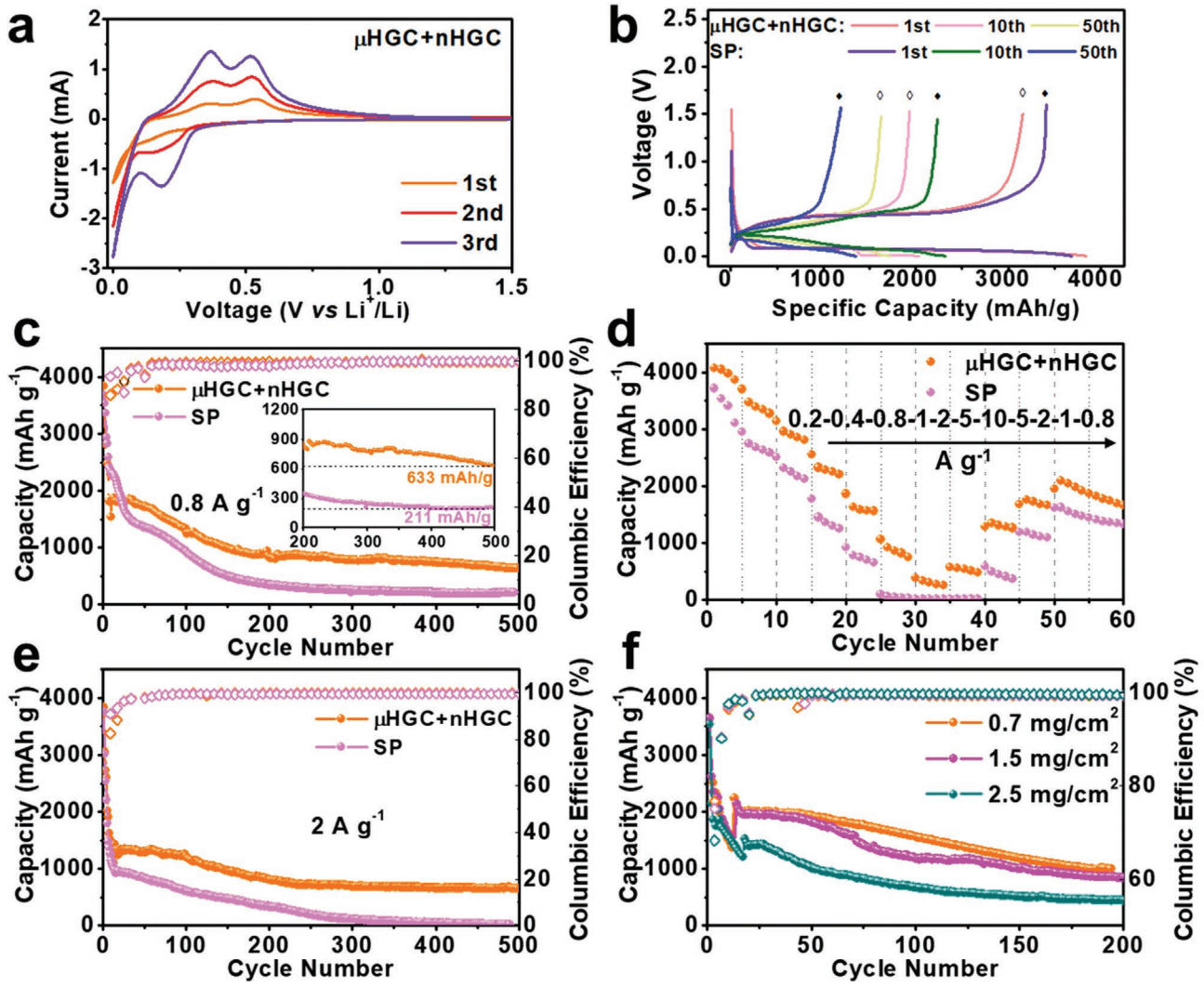

Figure 5. a) CV profile of the μHGC + nHGC@μSi anode. b) voltage profiles of the μHGC + nHGC@μSi and SP@μSi anodes at the 1st, 10th and 50th cycles. c) Long-term cycling performance at a current density of 0.8 A g^{-1} d) rate capability of the μHGC + nHGC@μSi and SP@μSi anodes. e) Long-term cycling performance at a high current density of 2 A g^{-1} and f) long-term cycling performances of the μHGC + nHGC@μSi anodes with different mass loadings.

voltage profiles of the μHGC@Si and nHGC@Si anodes are shown in Figure S7 (Supporting Information) for comparison. As shown in voltage profiles, the capacities of μHGC@Si and nHGC@Si anodes both exceed that of SP@μSi at the 50th cycle. Besides, μHGC@Si anode shows less capacity decay than nHGC@Si, which could be elucidated that μHGC plays a more critical role in regulating the large strain than nHGC.

Ultimately, we explored the long-term cycling performance of μHGC + nHGC@@μSi anode and compared the SP@μSi anode at a current density of 0.8 A g^{-1} over 500 cycles (Figure 5c). The μHGC + nHGC@μSi anode displays a lower initial Coulombic efficiency (ICE) of 85.9% than the SP@μSi anode (93.5%), which is mainly attributed to the high specific surface area of the μHGC and nHGC additives. Surprisingly, the Coulombic efficiency of the μHGC + nHGC@μSi anode exceeds that of the SP@μSi anode merely at the 4th cycle (96.63–95.9%). This can be explained as due to the μSi particles in the SP@μSi electrode facing more severe bulk pulverization, leading to more fresh surfaces being exposed to electrolyte and continuous SEI formation. By contrast, the volume variation of the μSi particles in the μHGC + nHGC@μSi electrode is alleviated by the elastic hollow graphitic structure of the μHGC and nHGC additives, thus better maintaining bulk integrity and exposing less surface to the electrolyte. Both electrodes display fast capacity decay during the first 200 cycles. However, it is important to highlight that the μHGC + nHGC@μSi anode still maintains a relatively high capacity of 828.2 mAh g^{-1}, whereas the capacity of the SP@μSi anode declines to 348.6 mAh g^{-1} which is even worse than that of commercial graphite. After 500 cycles, μHGC + nHGC@μSi anode manifests an outstanding capacity of 633 mAh g^{-1} that is far higher than that of the graphite anode, suggesting its commercial competitiveness. The inset in Figure 5c vividly shows the superiority of μHGC + nHGC@μSi anode after 200 cycles. By contrast, the capacity of the SP@μSi anode drops to 211 mAh g^{-1}, below the value necessary for practical use. Figure 5d shows the rate

capabilities of both anodes at various current densities. It is observed that the capability of μHGC + nHGC@μSi anode is comprehensively superior to that of the SP@μSi anode at all current densities. Furthermore, when tested at a high current density of 5 A g^{-1}, the μHGC + nHGC@μSi anode still obtains a capacity of 753.4–1066.7 mAh g^{-1} during five cycles, while the SP@μSi anode fails to work under such a high current. This huge difference can be ascribed to the μHGC and nHGC additives facilitating the construction of a more effective conductive network and a more stable electrode structure, as will be further discussed below. The cycling and rate performance of the μHGC@μSi and nHGC@μSi anodes are provided in Figure S8 (Supporting Information) for comparison. It shows that the μHGC + nHGC@μSi anode yields a higher reversible Li^+ storage capacity than the μSi anode constructed with only μHGC or nHGC after 150 cycles. Moreover, the μHGC+nHGC@μSi anode is capable of working under a high current density (5 A g^{-1}) and, again, provides excellent capacity when the current density returns to 0.8 A g^{-1}. In stark contrast, the μHGC@μSi and nHGC@μSi anodes fail to sustain rate tests. The long-term cycling performance of the batteries at a current density of 2 A g^{-1} is shown in Figure 5e to better confirm the superior rate capability of the μHGC+nHGC@μSi anode. Upon discharge and charge test for 500 cycles, the Li^+ storage capacity of the μHGC + nHGC@μSi anode first declines in the initial 200 cycles and then gradually attains a stable level of more than 651.4 mAh g^{-1} until the 500th cycle. By contrast, the capacity of the control SP@μSi anode continuously drops from the initial cycle and declines to ≈0 at ≈the 300th cycle. Figure 5f shows the performance of the μHGC + nHGC@μSi electrodes with different mass loadings of 0.7, 1.5, and 2.5 mg cm^{-2}, respectively. Only slightly lower capacity decay is observed when the electrode mass loading increases from 0.7 to 1.5 mg cm^{-2}, obtaining satisfactory capacities of 996.7 and 856.3 mAh g^{-1}, respectively. When the mass loading increases to 2.5 mg cm^{-2}, the performance shows a clear deterioration with a capacity retention of barely 438 mAh g^{-1}, demonstrating the limitation of the dual-size HGC additives to some extent. However, summarizing the performance of the μHGC + nHGC@μSi anode tested by the above methods, it can be affirmed that the dual-size HGC successfully improves the Li^+ storage performance of the μSi anode even by acting merely as conductive additives.

2.4. Structure and Kinetics Evolution

A series of electrochemical characterizations have convincingly elucidated the applicability of dual-size HGC as conductive additives in the μSi-based anode. The remarkable performance can be simply explained by two aspects: 1) the strain generated during lithiation is regulated and alleviated by the compressible HGC additives; 2) μHGC and nHGC additives synergistically build a robust conductive network that can withstand the continuous volume change. It has been confirmed by in situ TEM on a particle level that the hollow graphitic structures can be pressed under external pressure and then return to their original structure when withdrawing the pressure.[14] Here, we conducted ex-situ SEM and Raman spectroscopy on the electrode level to gain in-depth insight into the essential function of strain regulation, namely the alleviation of the μSi particle pulverization induced by Li^+ insertion and the reduction in the electrode expansion. **Figure 6**a,b shows the surface morphology of the μHGC + nHGC@μSi electrode in the fresh state and after 50 cycles, respectively. Only some slight cracks are observed in the aged electrode, illuminating the role of dual-size HGC in maintaining structural stability. By contrast, many huge cracks are observed in the aged SP@μSi electrode and a large area of active materials fell off the current collector and lost electrical connection during cycling tests as shown in Figure 6e,f. Furthermore, the thickness changes of the μHGC + nHGC@μSi electrode (Figures 6c,d) and the SP@μSi electrode (Figures 6g,h) were evaluated by cross-sectional imaging measurement for deep understanding. It was observed that the thickness variation of the dual-size-HGC-assisted electrode is much smaller than that of the conventional SP-assisted electrode, strongly supporting the above-mentioned role of strain regulation. Notably, the cross-sectional images also show that the active materials in the μHGC + nHGC@μSi electrode are still tightly attached to the current collector, while those in the SP@μSi electrode dramatically fall off. Figure S9 (Supporting Information) displayed the structure evolution of the μHGC@μSi electrode during the 50-cycle electrochemical test. The aged μHGC@μSi electrode shows very little cracks and quite small thickness change, confirming that μHGC manages to regulate the strain induced by lithiation. And Figure S10 (Supporting Information) showed the morphology of the nHGC@μSi electrode before and after cycling, in which serious thickness change is observed. Comparing the thickness evolution of the electrodes, it can be concluded that in dual-size HGC additives, μHGC works to regulate the strain of the electrode, and nHGC mainly works to build a more effective conductive network along with μHGC.

Ex situ Raman spectroscopy was employed to detect the structure evolution of the active materials and conductive additives in both electrodes. Figure 6i shows the Raman spectra of the fresh μHGC + nHGC@μSi and SP@μSi electrodes. A sharp and intense peak located at 520 cm^{-1} is observed in both electrodes, indicating the presence of crystalline Si. The Raman results for the carbonaceous additives in the electrodes contain a defect peak (1350 cm^{-1}) and characteristic peak (1580 cm^{-1}), and the intensity of the D/G peaks of the SP (1.28) additives is higher than that of the HGC additives (0.81), in agreement with the above findings. Figure 6j displays the Raman spectra of the μHGC + nHGC@μSi and SP@μSi electrodes after 50 cycles. It is observed that the characteristic peak of Si is considerably more intense in the aged μHGC + nHGC@μSi electrode than that in the aged SP@μSi electrode. This confirms that the dual-size HGC additives protect the μSi particle from pulverization and maintain its structural integrity, which cannot be realized by the commercial conductive additives SP. The peak at 520 cm^{-1} shifts to 475 cm^{-1} after 50 cycles, indicating that the crystalline Si was transformed to amorphous Si, in good agreement with the obtained CV profiles.[43] Moreover, the aged μHGC + nHGC@μSi electrode shows stronger peaks related to carbonaceous materials than the SP@μSi electrode, suggesting that HGC additives are more electrochemically and dynamically stable in the μSi electrode than the SP additives. In addition,

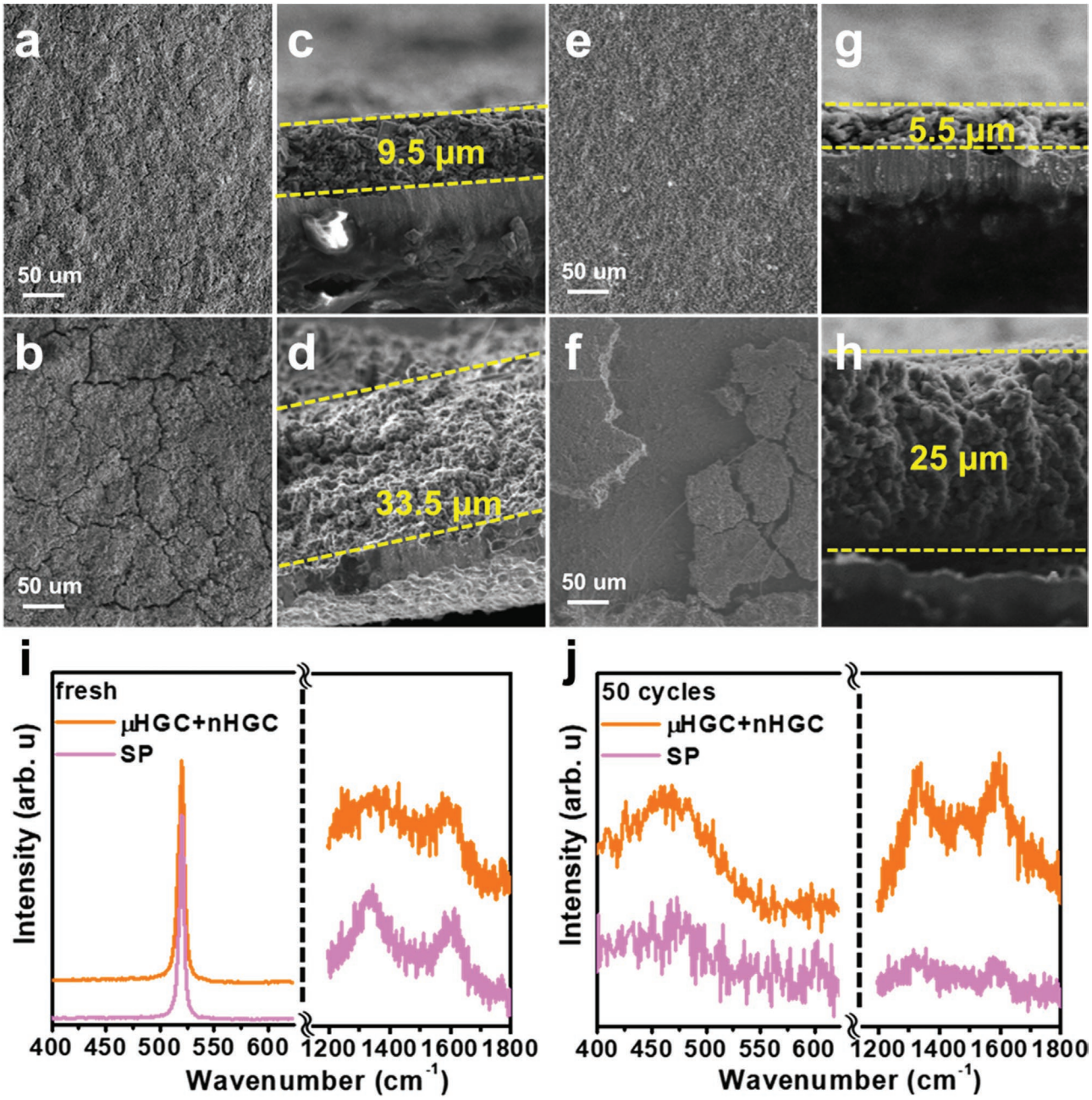

Figure 6. Surface morphology of the μHGC + nHGC@μSi electrode a) in the fresh state and b) after 50 cycles. Cross-section of the μHGC + nHGC@μSi electrode c) in the fresh state and d) after 50 cycles. Surface morphology of the SP@μSi electrode e) in the fresh state and f) after 50 cycles. Cross-section of the SP@μSi electrode g) in the fresh state and h) after 50 cycles. Raman spectra of the μHGC + nHGC@μSi and SP@μSi electrodes i) in the fresh state and j) after 50 cycles.

the D/G intensity ratio of dual-size HGC increases from 0.81 to 0.93, indicating a good structural integrity.

Various ex situ EIS measurements were carried out to illuminate the superior kinetics of the μHGC + nHGC@μSi anode. **Figure 7**a,b show the results of an ex situ EIS study of the μHGC + nHGC@μSi and SP@μSi anodes upon the first lithiation to 0.5, 0.2, 0.1, and 0 V. Comparison of the Nyquist plots in Figure 7a,b shows that the μHGC + nHGC@μSi anode exhibits smaller charger R_{ct} at an arbitrary lithiated state than the SP@μSi anode. The relationship between Z and $\omega^{-1/2}$ associated with Figure 7a,b at low frequencies is shown in Figure S11 (Supporting Information). The Warburg coefficients plotted in Figure S11 (Supporting Information) suggest that Li-ion transport is faster in the μHGC + nHGC@μSi electrode than in SP@μSi during the entire lithiation process. As a control, the results of the ex situ EIS measurements of the μHGC@μSi and nHGC@μSi anodes are plotted in Figure S12 (Supporting Information). The difference in the EIS results reveals that the

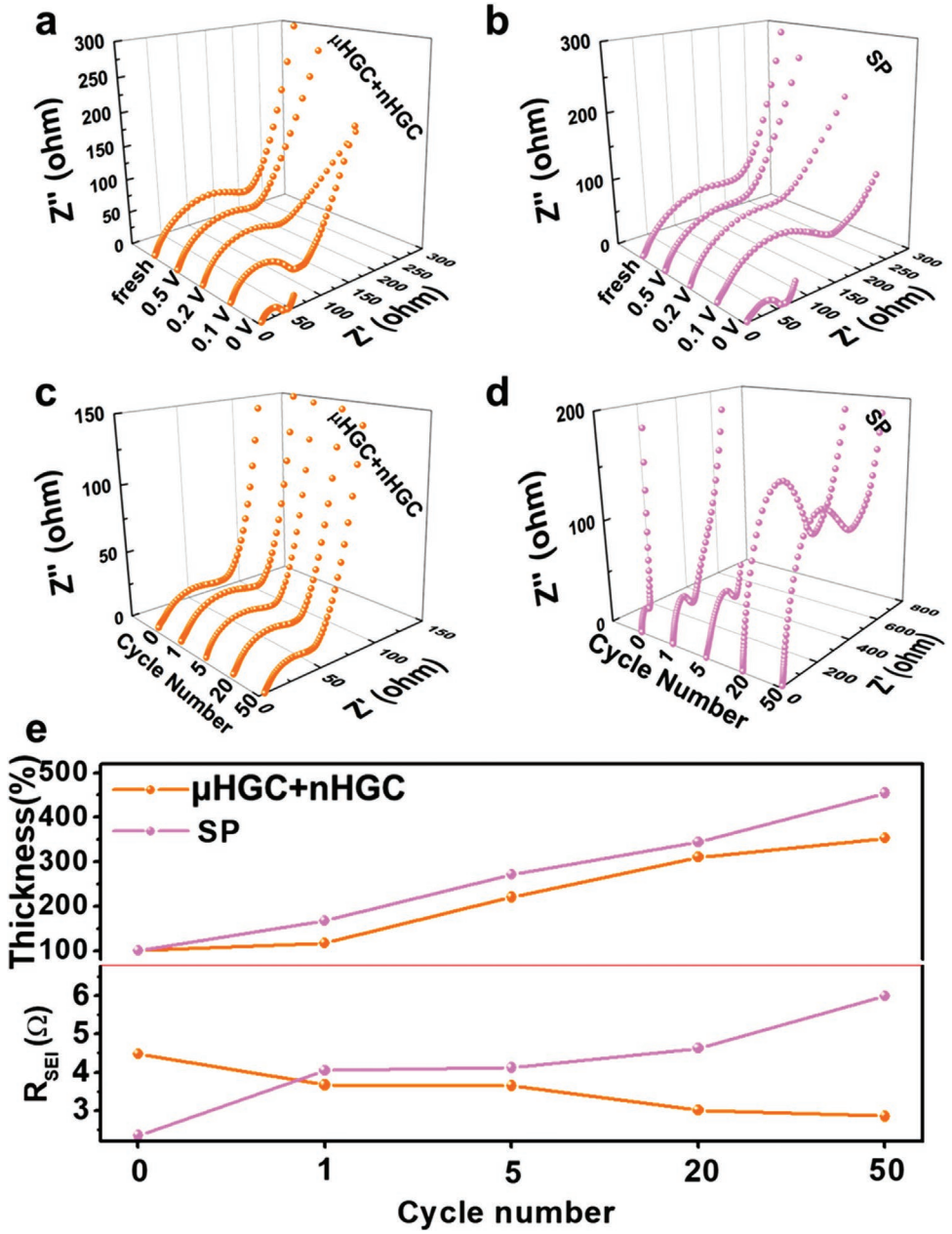

Figure 7. Ex situ EIS measurements of a) the μHGC + nHGC@μSi anode and b) the SP@μSi anode upon initial lithiation. Ex situ EIS measurements of c) the μHGC + nHGC@μSi anode and d) the SP@μSi anode in the fresh state, after 1 cycle, after 5 cycles, after 20 cycles, and after 50 cycles. e) Thickness change and R_{SEI} evolution of the μHGC + nHGC@μSi and SP@μSi electrodes in the fresh state, after 1 cycle, after 5 cycles, after 20 cycles, and after 50 cycles.

nHGC behaves better than μHGC in improving the electrical conductivity of the electrode. Ex situ EIS measurements carried out after testing the batteries for different numbers of cycles are displayed in Figure 7c,d. The resistance evolutions of the μHGC + nHGC@μSi and SP@μSi anodes as a function of the number of cycles show radically different trends. The R_{ct} of μHGC + nHGC@μSi anode increases slightly after the first cycle and then gradually decreases after 5, 20, and 50 cycles. This is because dual-size HGC additives regulate the lithiation-induced strain and result in the rearrangement of the electrode configuration, further leading to more intimate contact between the active materials and conductive additives. On the contrary, the impedance of the SP@μSi anode tends to increase with the number of cycles due to the degradation of the electrode structure.

The corresponding equivalent circuit derived from Figure 7c,d is displayed in Figure S13 (Supporting Information). The thickness variation statistics combined with R_{SEI} at certain cycles are shown in Figure 7e. It is observed that for both electrodes, the thickness increases after a certain number of cycles. However, the thickness of the μHGC + nHGC@μSi electrode increases less than that of SP@μSi. The corresponding

surface morphology and cross-sectional images are shown in Figures S14–S16. The R_{SEI} statistics for the SP@μSi anode presented in Figure 7e shows repeated increase because of the continuous SEI growth on the fractured Si surface that blocks ions transport. By contrast, the R_{SEI} of μHGC + nHGC@μSi anode tends to decrease from the initial cycle to the 50th cycle. It is speculated that few cracks are generated within the μSi particles during 50-cycle testing and HGC additives successfully construct an effective conductive network. Moreover, the R_{ct} of the SP@μSi anode increases strongly after a certain number of cycles as shown in Figure S17 (Supporting Information), but the R_{ct} of the μHGC + nHGC@μSi anode only shows a quite small enlargement. The data for the thickness change and the evolution of R_{SEI} and R_{ct} are presented in Table S1 (Supporting Information) in detail. Overall, the μSi anode with dual-size HGC additives exhibits a more stable structure and accelerated kinetics.

3. Conclusion

In this work, we have prepared dual-size hollow graphitic carbons and successfully employed them as conductive additives for μSi anodes. The dual-size HGC additives enable the μSi anode to obtain a smaller impedance than that of the commercial SP additives, delivering accelerated electron and ion transport as revealed by EIS measurements. As a result, the μHGC + nHGC@μSi anode obtains a reversible capacity of 633 mAh g^{-1} at 0.5 A g^{-1} and of 651.4 mAh g^{-1} at 2 A g^{-1} after 500 cycles. In particular, compared to the SP additives, the dual-size HGC additives greatly enhance the rate capability of the μSi anode. The excellent performance is further elucidated by ex-situ electron microscopy, combined with ex-situ EIS characterization and ex situ Raman spectroscopy. The various post-mortem analyses prove that dual-size HGC conductive additives play a significant role in regulating strain evolution and accelerating the reaction kinetics in the electrochemical process. This dual-size HGC can potentially be applied as advanced conductive additives for a range of alloy anodes such as Si and Sn anodes, without any additional modification.

Supporting Information

Supporting Information is available from the Wiley Online Library or from the author.

Acknowledgements

MHR thanks the National Natural Science Foundation of China (Grant Nos. 52071225 and 51672181), Department of Human Resources and Social Security of Jiangsu Province (100 Talents Project), the Czech Republic from ERDF "Institute of Environmental Technology–Excellent Research" (No. CZ.02.1.01/0.0/0.0/16_019/0000853) and the Sino-German Research Institute for their support (Project GZ 1400).

Open access funding enabled and organized by Projekt DEAL.

Conflict of Interest

The authors declare no conflict of interest.

Data Availability Statement

The data that support the findings of this study are available in the supplementary material of this article.

Keywords

dual-size conductive additives, hollow graphitic carbons, kinetics accelerating, micro-sized Si anodes, strain regulating

Received: August 28, 2022
Revised: November 1, 2022
Published online: November 26, 2022

[1] M. Li, J. Lu, Z. Chen, K. Amine, *Adv. Mater.* **2018**, *30*, 1800561.
[2] J.-M. Tarascon, M. Armand, *Nature* **2001**, *414*, 359.
[3] W. Wang, F. Xiong, S. Zhu, J. Chen, J. Xie, Q. An, *eScience* **2022**, *2*, 278.
[4] S. Liang, Y. Cheng, J. Zhu, Y. Xia, P. Müller-Buschbaum, *Small Methods* **2020**, *4*, 2000218.
[5] Y. Li, Y.-F. Du, G.-H. Sun, J.-Y. Cheng, G. Song, M.-X. Song, F.-Y. Su, F. Yang, L.-J. Xie, C.-M. Chen, *EcoMat* **2021**, *3*, e12091.
[6] J. Tang, X. Peng, T. Lin, X. Huang, B. Luo, L. Wang, *eScience* **2021**, *1*, 203.
[7] Q. Shi, J. Zhou, S. Ullah, X. Y. , K. Tokarska, B. Trzebicka, H. Q. Ta, M. H. Rümmeli, *Energy Storage Mater.* **2021**, *34*, 735.
[8] F. Xi, Z. Zhang, Y. Hu, S. Li, W. Ma, X. Chen, X. Wan, C. Chong, B. Luo, L. Wang, *J. Hazard. Mater.* **2021**, *414*, 125480.
[9] W. U. Rehman, H. Wang, R. Z. A. Manj, W. Luo, J. Yang, *Small* **2021**, *17*, 1904508.
[10] M. Ge, C. Cao, G. M. Biesold, C. D. Sewell, S. Hao, J. Huang, W. Zhang, Y. Lai, Z. Lin, *Adv. Mater.* **2021**, *33*, 2004577.
[11] P. Li, G. Zhao, X. Zheng, X. Xu, C. Yao, W. Sun, S. X. Dou, *Energy Storage Mater.* **2018**, *15*, 422.
[12] R. Andersson, G. Hernández, K. Edström, J. Mindemark, *Energy Technol.* **2020**, *8*, 2000056.
[13] M. A. Rahman, G. Song, A. I. Bhatt, Y. C. Wong, C. Wen, *Adv. Funct. Mater.* **2016**, *26*, 647.
[14] F. Chen, J. Han, D. Kong, Y. Yuan, J. Xiao, S. Wu, D. Tang, Y. Deng, W. Lv, J. Lu, F. Kang, Q. Yang, *Natl. Sci. Rev.* **2021**, *8*, 9.
[15] Z. Yi, N. Lin, Y. Zhao, W. Wang, Y. Qian, Y. Zhu, Y. Qian, *Energy Storage Mater.* **2019**, *17*, 93.
[16] W. An, B. Gao, S. Mei, B. Xiang, J. Fu, L. Wang, Q. Zhang, P. K. Chu, K. Huo, *Nat. Commun.* **2019**, *10*, 1447.
[17] Z. Zhang, Z. Wang, X. Lu, *ACS Nano* **2018**, *12*, 3587.
[18] X. Zhang, R. Guo, X. Li, L. Zhi, *Small* **2018**, *14*, 1800752.
[19] R. Yi, J. Zai, F. Dai, M. L. Gordin, D. Wang, *Nano Energy* **2014**, *6*, 211.
[20] B. Lee, T. Liu, S. K. Kim, H. Chang, K. Eom, L. Xie, S. Chen, H. D. Jang, S. W. Lee, *Carbon* **2017**, *119*, 438.
[21] J. Wang, Y. Cui, *Nat. Energy* **2020**, *5*, 361.
[22] J. Chen, L. Chen, X. Fan, X. Ji, Q. Li, C. Yang, H. Yang, M. R. Khoshi, H. He, O. Borodin, C. Wang, *Nat. Energy* **2020**, *5*, 386.
[23] T. M. Higgins, S. Park, P. J. King, C. Zhang, N. McEvoy, N. C. Berner, D. Daly, A. Shmeliov, U. Khan, G. Duesberg, V. Nicolosi, J. N. Coleman, *ACS Nano* **2016**, *10*, 3702.
[24] Z. Xu, J. Yang, T. Zhang, Y. Nuli, J. Wang, S.-I. Hirano, *Joule* **2018**, *2*, 950.
[25] C. Wang, H. Wu, Z. Chen, M. T. McDowell, Y. Cui, Z. Bao, *Nat. Chem.* **2013**, *5*, 1042.
[26] S. Choi, T. Kwon, A. Coskun, J. W. Choi, *Science* **2017**, *357*, 279.
[27] G. Xia, J. Ye, Z. Zheng, X. Li, C. Chen, C. Hu, *Carbon* **2021**, *172*, 96.

[28] K. Pfeifer, S. Arnold, O. Budak, X. Luo, V. Presser, H. Ehrenberg, S. Dsoke, *J. Mater. Chem. A* **2020**, *8*, 6092.
[29] X.-M. Fan, X.-H. Zhang, G.-R. Hu, B. Zhang, Z.-J. He, Y.-J. Li, J.-C. Zheng, *Ionics* **2020**, *26*, 1721.
[30] Y. Li, Y. Chen, W. Feng, F. Ding, X. Liu, *J. Power Sources* **2011**, *196*, 2246.
[31] Y. Shi, L. Wen, S. Pei, M. Wu, F. Li, *J Energy Chem* **2019**, *30*, 19.
[32] L. Xu, W. Lv, K. Shi, S. Xiao, C. You, Y. He, F. Kang, Q.-H. Yang, *Carbon* **2019**, *149*, 257.
[33] D. Ozgit, P. Hiralal, G. A. J. Amaratunga, *ACS Appl. Mater. Interfaces* **2014**, *6*, 20752.
[34] A. Rezqita, R. Hamid, S. Schwarz, H. Kronberger, A. Trifonova, *ECS Trans.* **2015**, *66*, 17.
[35] Y. Wang, D. Zhao, K. Zhang, Y. Li, B. Xu, F. Liang, Y. Dai, Y. Yao, *J. Energy Storage* **2020**, *28*, 101182.
[36] H. Zhang, S. Liu, X. Yu, S. Chen, *J. Alloys Compd.* **2020**, *822*, 153664.
[37] C. Lu, Z. Sun, L. Yu, X. Lian, Y. Yi, J. Li, Z. Liu, S. Dou, J. Sun, *Adv. Energy Mater.* **2020**, *10*, 2001161.
[38] L. Song, S. Xin, D.-W. Xu, H.-Q. Li, H.-P. Cong, S.-H. Yu, *ChemNanoMat* **2016**, *2*, 540.
[39] Z. Jiang, Z.-J. Jiang, X. Tian, L. Luo, *Electrochim. Acta* **2014**, *146*, 455.
[40] B. Li, W. Zhao, Z. Yang, C. Zhang, F. Dang, Y. Liu, F. Jin, X. Chen, *J. Power Sources* **2020**, *466*, 228339.
[41] N. Ding, J. Xu, Y. X. Yao, G. Wegner, X. Fang, C. H. Chen, I. Lieberwirth, *Solid State Ionics* **2009**, *180*, 222.
[42] Q. Shi, H. Wang, J. Zhou, H. Q. Ta, J. Wang, X. Lian, K. Kurtyka, B. Trzebicka, T. Gemming, M. H. Rümmeli, *Nano Res.* **2022**, *15*, 8146.
[43] M. Shimizu, H. Usui, T. Suzumura, H. Sakaguchi, *J. Phys. Chem. C* **2015**, *119*, 2975.